In operando monitoring of wood transformation during pretreatment with ionic liquids

Jörn Viell [iD] · Noemi K. Szekely · Gaetano Mangiapia [iD] · Claas Hövelmann ·
Caroline Marks [iD] · Henrich Frielinghaus [iD]

Abstract The conversion of lignocellulosic biomass or wood into chemicals still poses a challenge due to the recalcitrance of this composite-like material consisting of lignin, hemicellulose and cellulose. A very high accessibility of cellulose is reported by a pretreatment with ionic liquids that enables high conversion rates by enzymatic hydrolysis. However, the underlying mechanisms have not yet been monitored in operando nor are they fully understood. We monitored the transformation of wood in ionic liquids using small-angle neutron scattering to observe changes in the material in operando and to elucidate the intrinsic effects. The data analysis shows three different stages that is (1) impregnation, (2) the formation of voids and (3) increasing structure size within cellulose fibrils. This consecutive mechanism coincides with macroscopic disintegration of the tissue. The analysis further reveals that the reduction of order in longitudinal direction along the fiber axis is a prerequisite for disintegration of cells along the radial direction. This understanding supports further research and development of pretreatment processes starting from lignocellulosic raw material.

J. Viell · C. Marks
Aachener Verfahrenstechnik - Process Systems Engineering, RWTH Aachen University, Forckenbeckstr. 51, 52074 Aachen, Germany

N. K. Szekely · C. Hövelmann · H. Frielinghaus (✉)
Forschungszentrum Jülich GmbH, Jülich Centre for Neutron Science At MLZ, Lichtenbergstrasse 1, 85747 Garching, Germany
e-mail: h.frielinghaus@fz-juelich.de

G. Mangiapia
Helmholtz-Zentrum Geesthacht GmbH, German Engineering Materials Science Centre At MLZ, Lichtenbergstr. 1, 85748 Garching, Germany

Graphic abstract
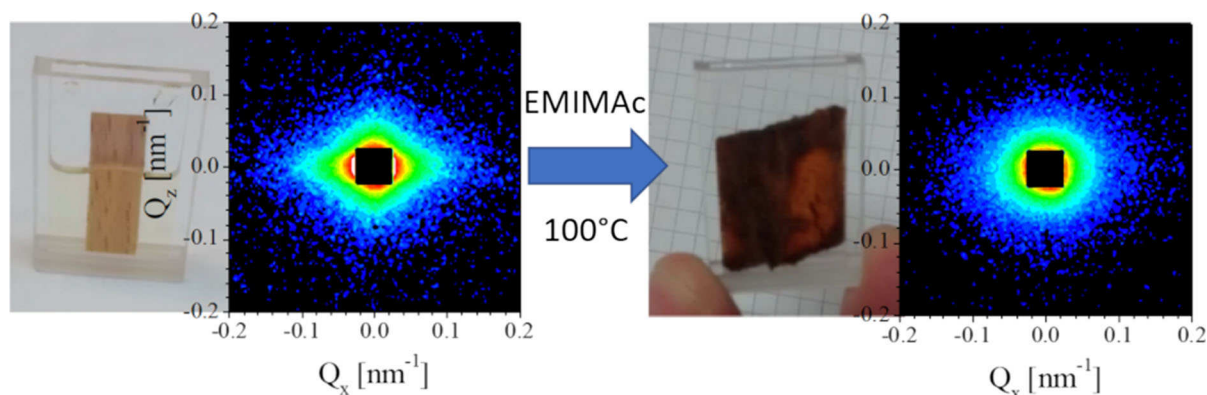
Introduction

One promising but challenging source for the production of chemicals is lignocellulose or wood. It is abundant and not in direct competition with food supply. However, the semi-crystalline cellulose that is organized in fibrils and embedded in the matrix components lignin and hemicellulose forms a composite-like structure. It exhibits a strong recalcitrance against biological, mechanical or chemical attack. The conversion of the constituting polymers thus requires a process step called pretreatment.

The pretreatment itself involves several physicochemical changes (Mosier et al. 2005). Crystallinity and the molecular accessibility of the cellulose macromolecules are the most promising parameters in view of a subsequent digestibility of the cellulose by enzymes. These parameters point to the larger nanometer scale, which constitutes polymers and its 3D-intercalation. In contrast, the efficiency of pretreatment is usually characterized by comparison of the processed material with its native form and by analyzing the liquid products. Hence, pretreatment in particular lacks research and analysis in operando.

The pretreatment provides the raw material for a broad product range. In the simplest case, the cellulose can be hydrolyzed to glucose that can be converted to a fuel such as ethanol (Lee et al. 2009). Nevertheless, glucose and oligomers can be used to produce

detergents (Billès et al. 2016), modified polysaccharides (Niaounakis 2013) and monomers, (Niaounakis 2013) such as 3-hydroxybutyrate-co-4-hydroxybutyrate, tri-methylene terephthalate for polymerization. Even polyurethanes can be produced from cellulose oligomers without modifications (Niaounakis 2013). Moreover, lignin can be used possibly to produce carbon fibers (Baker and Rials 2013) and can be mixed with Bakelite (Niaounakis 2013) or thermoplasts (Mohanty et al. 2003; Tecnaro 2019). Further chemo- or biocatalytic upgrading into functional molecules of higher value is the subject of many research activities. However, pretreatment is the key of all these value chains from woody material.

An interesting pretreatment concept deals with ionic liquids (ILs). It requires only modest temperature at atmospheric pressure and the pretreated biomass shows nearly complete accessibility to enzymes. The most studied IL is 1-ethyl-3-methylimidazolium acetate or EMIMAc (Viell et al. 2016; Zhang et al. 2005; Moulthrop et al. 2005; Sun et al. 2009) for different reasons: (a) The conversion reaches for extremely high contents of amorphous cellulose (Viell et al. 2016; Lee et al. 2009), which enables yields in enzymatic hydrolysis of more than 90 wt%. (b) The non-volatile nature of ionic liquids can lead to very high recycling rates (Lee et al. 2009). Clearly, high recycling rates are also required due to the high cost of ILs but the negligible vapor pressure also facilitates lab handling as any dissolved fraction in the IL can be precipitated by water dilution and subsequent washing. This way, the cellulose and oligomers are obtained as fluffy "solid" material after the pretreatment. (c) Rather low temperatures of around 110 °C

involve little side-reactions that might form inhibitors and reduce the yield from cellulose and lignin (Viell et al. 2016; Lee et al. 2009). In sum, ILs pose an interesting concept as they warrant maximum value at mild conditions in the yet rather poorly understood pretreatment of wood.

One important detail of the IL treatment is the change of the ultrastructure of lignocellulose. The increased accessibility for enzymes seems to be strongly related to the cellulose structure that is the arrangement of cellulose chains in the cell wall and the cellulose crystallinity. In fact, cellulose can be transformed from natural cellulose I to the thermodynamically more stable cellulose II (Kontturi 2006; Song et al. 2015). In particular alkaline conditions eventually lead to the rearrangement of neighboring cellulose fibers with different orientation to form cellulose II. Along with this transformation, the cellulose is often (partially) in an amorphous state (Song et al. 2015). Both the cellulose II and the amorphous state give much better access to the enzymes for the hydrolysis (Pihlajaniemi et al. 2015; Wada et al. 2010), while crystalline fractions embedded in lignin and hemicellulose inhibit or decelerate the full enzymatic conversion to oligomeric sugars. Anyhow, the precise interaction of solvents, cellulose and lignocelluose in particular is still unclear (Li et al. 2018; Chen et al. 2018).

Small-angle neutron scattering (SANS) has been applied to study numerous materials ranging from polymers to composite materials (Feiging and Svergun 1987) and even enzymes (Pingali et al. 2011). Often the method deals with disorder arising from the system or due to orientational disorder. The resolution of the instrument is often relaxed to enhance resolution at the nanometer-scale. This enables a structural analysis on mesoscopic length scales to which a lot of methodological efforts need to be paid. In this way, the dimensions of microfibrils as structural element of the native ultrastructure have been identified (Fernandes et al. 2011). The distance between intact fibrils varies due to humidity that induces swelling of the material (Plaza et al. 2016). The latter process has been observed in situ during drying.

The changes during pretreatment have been addressed in first reports using SANS. An analysis of pretreatment using steam explosion (Langan et al. 2014) or dilute acid (Pingali et al. 2010a, b) shows that microfibrils coalesce after interfibrillar water and hemicellulose have been removed. The size of crystalline cellulose even increased by these kind of pretreatments (Nishiyama et al. 2014). Additionally, it is known that lignin strongly tends to form aggregates during such processes (Petridis et al. 2011). In contrast to steam explosion or dilute acid, ionic liquids dissolve some matrix polysaccharides and the cellulose structure but at much lower temperature. Recent studies of the material before and after pretreatment in IL suggest a mixed effect of increased porosity and reduced crystallinity (Wang et al. 2018). An in operando analysis of a wood pretreatment with ionic liquids is not known to the authors.

In a previous study, we have shown that water contents of up to 8.6 wt% in the IL EMIMAc do not dramatically change the pretreatment process, while higher dilution reduces the activity of the IL that reduces the swelling and disintegration of the tissue and the accessibility in subsequent enzymatic hydrolysis dramatically (Viell et al. 2016). Thus, there seems to be a threshold that determines some molecular change to increase accessibility of cellulose in the ionic liquid. In this contribution, we present an in operando study of the pretreatment of beech wood in the ionic liquid EMIMAc. After macroscopic investigation by microscopy, we apply small-angle neutron scattering to reveal structural changes of the material that lead to macroscopic disintegration. The changes in anisotropy are analyzed quantitatively by a simple model and also by a detailed analysis in order to clarify the structural changes monitored in operando by SANS on the nm-level.
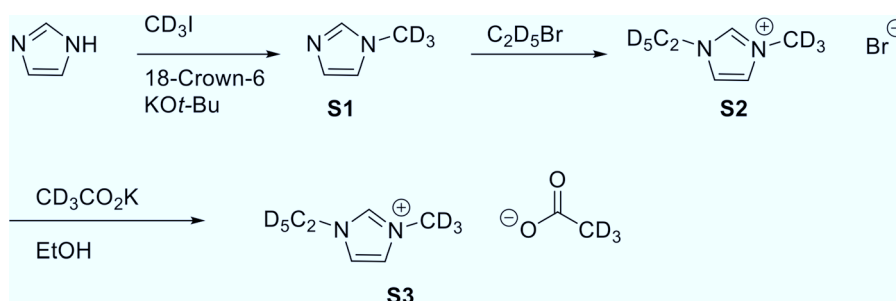
Materials

Microscopic analyses were carried out using commercial 1-ethyl-3-methylimidazolium acetate (EMIMAc) produced by Iolitec.

Synthesis of deuterated EMIMAc

1-(1,1-^{2}H-2,2,2-^{2}H)-Ethyl-3-(1,1,1-^{2}H)-Methyl-imidazolium (1,1,1-^{2}H)-acetate (see Fig. 1).

1-(1,1,1-^{2}H)-methylimidazole (S1)

10.6 g imidazole (156 mmol), 4.1 g 18-crown-6 and 19.3 g KO-tBu were introduced in a 500 ml three-

Fig. 1 Scheme of the synthesis of deuterated EMIMAc

necked flask. The flask was evacuated and 200 ml dry Et$_2$O were added under a stream of argon. The solution was stirred for 20 min and cooled to 0 °C. 22.6 g MeI-d$_3$ in 100 ml dry Et$_2$O were slowly added over the course of 1 h via an addition funnel. The reaction was allowed to warm to room temperature and stirring was continued overnight. The mixture was filtered over a glass frit and the precipitate was washed with 300 ml Et$_2$O. The solvent was removed under reduced pressure and the remaining residue was distilled at 20 mbar to yield 6.66 g (50%) pure N-methylimidazole as the main fraction at 83 °C.

1,1-^{2}H-2,2,2-^{2}H-ethylbromide

21.95 g ethanol-d$_6$, 41 ml H$_2$O and 53 g KBr were introduced into a 250 ml round bottom flask equipped with a reflux condenser. The solution was cooled to 0 °C and 59 ml conc. H$_2$SO$_4$ was added through the condenser over the course of 1 h. The temperature was slowly raised up to 73 °C and the product was refluxed for 20 min before the product was collected. Then, the temperature was slowly raised to 90 °C and the product was collected and cooled to 0 °C. The main fraction was extracted with conc. H$_2$SO$_4$ (2 × 10 ml), H$_2$O (10 ml), saturated Na$_2$CO$_3$ solution (10 ml) and again 10 ml H$_2$O to yield 32.96 g (69%) bromoethane-d$_5$.

Potassium acetate-d$_3$

A K$_2$CO$_3$ solution was prepared from 12 g K$_2$CO$_3$ and 15 ml D$_2$O. The mixture was warmed to obtain a clear solution. The K$_2$CO$_3$ solution was slowly added to 11.2 g deuterated acetic acid (AcOH-d$_4$) at 0 °C until the gas evolution ceased. The addition was monitored to avoid an excess of carbonate. D$_2$O was removed in

vacuo and the remaining colorless solid was further dried under high vacuum conditions for 3 d to yield 13.535 g (76.5%) of 1,1,1-^{2}H-potassium acetate.

1-(1,1-^{2}H-2,2,2-^{2}H)-ethyl-3-(1,1,1-^{2}H)-methyl-imidazolium bromide (S2)

6.66 g (77.4 mmol) 1-(1,1,1-^{2}H)-Methylimidazole were dissolved in 40 ml dry cyclohexane. 13.226 g (116 mmol) 1,1-^{2}H-2,2,2-^{2}H-Ethylbromide were added dropwise at 0 °C. The reaction was stirred at room temperature overnight and then heated to 80 °C for 24 h. After cooling to r.t. the solvent was decanted and the slightly yellow solid was washed with additional 20 ml of cyclohexane. The product was dried at 90 °C for 2 days under high vacuum conditions to yield 14,75 g (96%) of 1-(1,1-2H-2,2,2-2H)-Ethyl-3-(1,1,1-2H)-Methyl-imidazolium bromide.

1-(1,1-2H-2,2,2-2H)-ethyl-3-(1,1,1-2H)-methyl-imidazolium (1,1,1-2H)-acetate (S3)

14.75 g 1-(1,1-2H-2,2,2-2H)-Ethyl-3-(1,1,1-2H)-Methyl-imidazolium bromide were dissolved in 100 ml ethanol. 5.138 g KOAc-d$_3$ was added and the mixture was stirred for 6 h at 40 °C and overnight at room temperature. The suspension was filtered over a glass frit, the solvent was removed under reduced pressure and the remaining residue was dried for 1 h under high vacuum conditions. 30 ml cold dichloromethane were added while stirring at 0 °C for 10 min. The suspension was again filtered over a glass frit and the solvent was removed in vacuo. ^{2}H-NMR analysis of the product showed a degree of deuteration of 60% for the acetate compared to the aliphatic protons. Therefore the acetate exchange was repeated using 3 g KOAc-d$_3$ in 50 ml EtOH using the

same sequence as described above. The resulting yellow liquid was dried at 60 °C for 2 days under high vacuum conditions to yield 12.2 g (91%) of 1-(1,1-2H-2,2,2-2H)-Ethyl-3-(1,1,1-2H)-Methyl-imidazolium (1,1,1-2H)-acetate. ^{2}H-NMR analysis confirmed equimolar amounts of Me-d$_3$, Et-d$_5$, and OAc-d$_3$. All deuterated groups showed a residual proton content of below 0.3%.

Beech wood was received from local hardware shops as 5 mm × 5 mm rectangular rod for microscopy and as veneer of 1 mm thickness (Karl Kohl GmbH, Cologne, Germany) for in operando SANS measurements. The veneer was cut in rectangular chips (approx. 2 mm × 10 mm). In dedicated samples, preferentially lignin was removed according to the method by Ebringerová and Hromadková (1989) with NaOCl (12% active chlorine) acidified with acetic acid to pH < 5 for 2 h at 70 °C. Afterwards the pretreated wood chips were washed with water and dried in vacuum overnight at room temperature. A gravimetric analysis showed the removal of 38% dry matter. The chips retained their macroscopic structure without disintegration. Raman spectra show that most of the lignin is removed (Fig. 12 in Supplementary Information, SI).

NaOD (40 wt% in D$_2$O) was purchased from Sigma Aldrich, Darmstadt, Germany and used as received. Heavy water was purchased form Armar Chemicals, Döttingen, Switzerland and used as received.

Methods

Microscopy

Beech wood was cut with a sled microtome to 60 μm thick cross sections. The cutting direction was thus radial with respect to the growth direction. The section was investigated in transmission mode in a heating stage (Linkam LTS120) which was fixed under a microscope (Wild Stereomikroskop). Before the actual experiment, the coverglass (12 mm × 12 mm) with the sample underneath was fixed on an object slide with a droplet of the liquid to ensure that the wood sample did not slip out of position during the experiment and especially when adding the liquid. 10 μl of EMIMAc were sufficient to achieve complete filling of the sample and the void between coverglass and object slide. Pictures were recorded automatically

(ColorViewXS). The experiments were carried out at 95 °C. The effect of alkali cannot be monitored this way because of evaporation.

SANS

In operando small-angle neutron scattering (SANS) experiments have been conducted on the instrument KWS-1 (Feoktystov et al. 2015; Frielinghaus et al., 2015) at the Heinz-Maier-Leibnitz Zentrum with the FRM-2 research reactor. The neutron wavelength was λ = 0.5 nm. The sample cells were of 1 mm thickness with a maximum amount of wood in between, and were proof for 10 bar pressure (see Fig. 9 in SI). Alternatively, some of the IL treatments have been performed in an open cell (cf. table-of-content figure). The cell temperature was 100 °C for all measurements. The nominal detector distances of 20 m, 4 m and 1.5 m were used (the actual detector distances were 0.4 m shorter) with typical acquisition times from 5 and 10 min in the beginning to 20 and 30 min at the end of the in operando observation. For all detector distances, a new sample has been prepared. All data have been corrected for the 1 mm empty cell scattering, transmission, and detector efficiency using a secondary Plexiglas® standard. The intensities are represented as a function of the scattering vector $Q = (4\pi/\lambda)\sin(\theta/2)$ with θ being the geometric scattering angle. The pretreatment often caused a disintegration of the wood, such that the obtained intensities are quantitative if interpreted in terms of absolute scattering power dΣ/dΩ (in cm^{-1}).

The interpretation of complex SANS data requires models of which parameters refer to structural length scales at a given resolution. The resolution of a SANS experiment was properly described by Pedersen et al. (1990) according to:

$$\frac{\sigma_Q^2}{Q^2} = \frac{1}{8\ln2}\left(\frac{\Delta\lambda^2}{\lambda^2} + \frac{1}{4\theta^2}\left[\frac{d_C^2}{L_C^2} + d_S^2\left(L_C^{-1} + L_D^{-1}\right)^2 + \frac{d_D^2}{L_D^2}\right]\right)$$

(1)

with Δλ being the full width at half maximum of the wavelength distribution, d_C, d_S, and d_D being the diameters of the entrance (collimation) aperture, of the sample aperture and the detector element (in the sense of spatial resolution), and L_C and L_D being the

collimation and detector distances. In terms of neutron coherence in the scattering plane the following coherence length can be defined:

$$\xi_{\text{coh}} = \frac{\pi^2}{16\sqrt{2\ln 2}} \sigma_Q^{-1} \qquad (2)$$

For 1.5 m and 4 m detector distance, the typical coherence lengths of 4 and 13 nm would be obtained. When the sample system also displays a finite correlation length ξ_{sys} (according to the spatial van Hove correlation function), the overall maximum correlation length ξ_{tot} that can be observed by the scattering experiment is determined by:

$$\xi_{\text{tot}}^{-2} = \xi_{\text{coh}}^{-2} + \xi_{\text{sys}}^{-2} \qquad (3)$$

In wood, the length scales are ranging up to micrometers (Fengel and Wegener 1989). Thus, the sample system correlation length is often small and $\xi_{\text{tot}} = \xi_{\text{coh}}$. Hence, the largest structural sizes of the 1.5 m and 4 m measurements are 4 and 13 nm. This range applies to the equatorial and meridional directions that appear for a wood sample that is aligned vertically with its growth direction.

SANS modeling

The structure of cellulose and progress of pretreatment were monitored at three detector distances to resolve different length scales of cells, fibril alignment and cellulose structure. The following section describes the models for data evaluation that have been developed to exploit the measurements. Figure 2 shows the considered scattering geometry in the model. Most pronounced is the scattering of cells and fibrils. The latter occur mainly in the secondary wall layers. Hence, we describe the experimental scattering as a superposition of the cell wall scattering at very large scales and a scattering contribution at the level of the fibrils with cylindrical shape. For the cylindrical structures on the fibril level there is a radius R and a length L. In the following, we first present a detailed model including these structures. Second, we suggest a reduced model for fast and easy analysis of pretreatment in operando.

Reduced model

At 20 m, one mainly observes the Porod scattering from the cell walls against the rather empty cells that are then flooded by the deuterated IL. The anisotropy arises from the preferential growth direction along the longitudinal axis. As most of the cell walls in the experiment are oriented vertically along the growth direction, they give rise to scattering in the meridional direction. In contrast, the adjacent cells that are interconnected with pits and close cells in the growth direction give rise to scattering in the equatorial direction. The general layout of the two superimposed scattering patterns resembles the scattering of ramie fibers (Nishiyama et al. 2003) with the extension of the scattering pattern perpendicular to the fibers. Overall, the Porod scattering has a Guinier range—a rather flat scattering feature—that crosses over to the characteristic Q^{-4} power law at a $Q_c \approx 2\pi/R_c$ connected to the characteristic size of the cell walls R_c in the micrometer range. This cross over is far out of the SANS range, and, therefore, is not observed directly. However, if the amplitude of the scattering feature is large, the Porod Q^{-4} scattering pattern prevails even at much higher Q in the SANS range. From the scale of the Porod scattering (Nishiyama et al. 2014) the characteristic size R_c can be extrapolated, and we arrive in the 100 μm range. This coincides with the lumen size. So the surface of the lumen versus the cell walls (with a lumen-lumen distance of 2–10 μm) is observed (Penttilä et al. 2019). All of this gives rise to a fraction of scattering with fourfold symmetry. This fraction of well-ordered cell walls is measured with the established order parameter P_4 with values between 1 and − 1 (1 for highly aligned patterns along equatorial and meridional axis, and − 1 for scattering pattern turned by 45°):

$$P_4 = \frac{\iint dr\, d\varphi\, I(r, \varphi) \cos(4\varphi)}{\iint dr\, d\varphi\, I(r, \varphi)} \qquad (4)$$

Since the equatorial scattering prevails a little, a weaker contribution of a twofold symmetry order parameter P_2 is to be expected (between 1 and − 1, 1 for strong equatorial scattering and − 1 for strong meridional scattering):

$$P_2 = \frac{\iint dr\, d\varphi\, I(r, \varphi) \cos(2\varphi)}{\iint dr\, d\varphi\, I(r, \varphi)} \qquad (5)$$
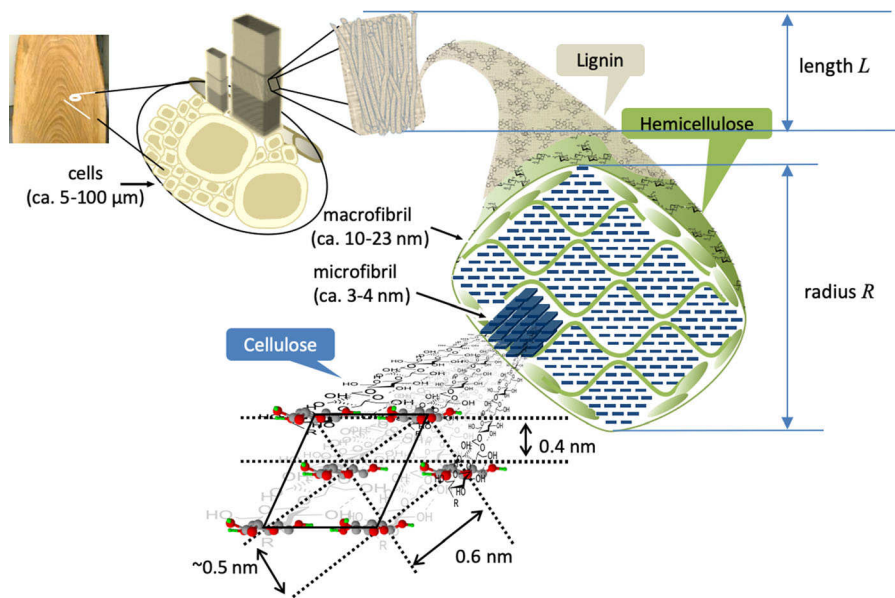
Fig. 2 Geometry of the wooden structure evaluated in this work (representative lengths are given from Fengel and Wegener 1989). Cells and fibrils mainly from the S2 layer of the cell wall are suggested to contribute to scattering. Using SANS we aim at the fibril radius R in the nanometer range. The cell wall thickness L_{eq}, i.e. the lumen–lumen distance, is in the range of 2 µm and the fibril length L in the range of 5 µm. Both lengths are only seen indirectly. The SANS experiments are carried out so that the meridional direction in the experiments is along the cell wall axis (vertical), while the equatorial direction is transverse to the cells (horizontal)

The angle φ is zero along the equatorial direction to the right. All integrals are carried out over the whole active detector area.

Detailed model

For the shorter detector distances of 1 and 4 m, the cellulose structure becomes dominant, Hence, any model must consider aligned fibrils. The scattering of this scenario can be described by a 2-dimensional hard cylinder (or disc) Perkus–Yevick (Rosenfeld 1990; Börner et al. 2008) structure factor S according to:

$$S_{PY}^{-1}(Q,R,\eta)$$
$$= 1 + 4\eta\left\{\left[A\frac{J_1(QR)}{QR} + BJ_0(QR)\right] \cdot \frac{J_1(QR)}{QR} + G\frac{J_1(2QR)}{QR}\right\} \tag{6}$$

with the Bessel functions $J_0(x)$ and $J_1(x)$, and the coefficients:

$$A = \left[1 + \frac{(2\eta - 1)}{(1 - \eta)^2} + 2\eta G\right]/\eta \tag{7}$$

$$B = \left[\frac{1}{(1 - \eta)} - 1 - 3\eta G\right]/\eta \tag{8}$$

$$G = (1 - \eta)^{-3/2}. \tag{9}$$

In case of wood, we interpret the two parameters R and η in the following meaning: R is the microfibril radius, and η is the microfibril concentration within the cell wall. The latter is a local concentration of cylinders η that describes the effect of no overlap on the local scale derived from a thermodynamic model (Rosenfeld 1990; Börner et al. 2008). In principle, different structure factors have also been applied elsewhere (Penttilä et al. 2019) with a different understanding of disorder that in our case only appears due to a finite local concentration η. The fibril complex scattering thus combines to the following:

$$\frac{d\Sigma_{fibril}}{d\Omega}(\boldsymbol{Q}) = \underbrace{(\Delta\varrho^2\phi\eta(1 - \eta) \cdot \pi R^2 L)}_{A_{fibril}} \cdot S_{PY}(Q_{xy},R,\eta)$$
$$\cdot \left(2\frac{J_1(Q_{xy}R)}{Q_{xy}R}\right)^2 \left(\frac{\sin(Q_z L/2)}{Q_z L/2}\right)^2. \tag{10}$$

The first bracket includes a prefactor $A_{fibril} = \Delta\rho^2\phi$ $\eta(1 - \eta)\pi R^2 L$ that depends on the contrast, which is determined by the scattering length density difference $\Delta\varrho^2$ between the fibril and the surrounding liquid (water and/or the ionic liquid), by the concentration ϕ of fibrils in the overall wood and by the concentration η of microfibrils in a fibril. This prefactor hardly can be split into its single factors in experiments with natural materials. So, we take it as one fitting parameter determined by the experiment. The second factor in Eq. (10) is the structure factor taking the interactions of fibrils into account. The third factor describes the cross section in the equatorial direction and assumes a simple circular shape. The last bracket is typically connected to meridional fibril length L in the range of μm to mm. Due to this large dimension of the parameter L, it oscillates heavily in the SANS-Q-range. There are two effects of the finite resolution: (a) the oscillations are smeared out and remain invisible. (b) The total width of the residual function is dominated by the resolution. Only from the amplitude of the scattering terms the scattering volume remains visible. Consequently, the last scattering term $(\sin(Q_Z L/2)/(Q_Z L/2))^2$ is then written as $(1 + (Q_z\xi_{tot,Z})^2/2)^{-1}$ with ξ as the coherence length in the following. This replacement of the large length scales (of μm size) by the coherence length of a few nanometers size are a feature of the scattering method. The length parameter in the scattering volume can be interpreted as a free length (persistence length) in the branched network of fibrils.

At 1 and 4 m, the cell wall scattering has been superimposed to the fibril scattering and was modeled by:

$$\frac{d\Sigma_{\text{wall}}}{d\Omega}(\boldsymbol{Q}) = \underbrace{\left(\Delta\varrho^2_{\text{wall}}\phi V_{\text{wall}}\right)}_{A_{\text{wall}}} \cdot \frac{1}{1 + Q^2_{xy}\xi^2_{\text{tot,xy}}/2}$$
$$\cdot \frac{1}{1 + Q^2_z\xi^2_{\text{tot,Z}}/2}. \qquad (11)$$

Again, the prefactor $A_{\text{wall}} = \Delta\rho^2_{\text{wall}} \phi V_{\text{wall}}$ is a single fitting parameter which hardly can be split in its single contributions. Again, the instrumental resolution dominates the Q-dependence of the scattering distribution. For a better representation of the scattering data we distinguished $\xi_{\text{tot,xy}}$ and $\xi_{\text{tot,Z}}$. For small Q, the classical Q^{-4} Porod scattering is obtained due to a slight averaging of the axis orientation by $\pm$ 5°.

The two contributions of Eqs. (7) and (8) and the incoherent background are superimposed to describe the scattering patterns at 1 and 4 m detector distance. So we arrive at:

$$\frac{d\Sigma}{d\Omega}(\boldsymbol{Q}) = \frac{d\Sigma_{\text{fibril}}}{d\Omega}(\boldsymbol{Q}) + \frac{d\Sigma_{\text{wall}}}{d\Omega}(\boldsymbol{Q}) + \{\text{background}\}.$$
$$(12)$$

This model can now be used to evaluate the 2-dimensional scattering intensities of the shorter detector distances.

Results

Microscopy

The microscopic images taken during treatment of radial wood cuts in EMIMAc show different stages of wood disintegration (Fig. 3). Initially, the wood rays and the difference between earlywood and latewood is clearly visible. Although individual cells of the tissue cannot be resolved at this resolution, numerous vessel cells can be recognized by their large lumen (appearing as bright dots in the picture). The lumen is approximately 35.7–60 μm wide with a distance across cell walls of approx. 2.2 μm. This agrees well to cell wall thickness reported in literature of 1 μm (Fengel and Wegener 1989). Consequently, the smaller fibres are anticipated to have an open lumen of 1 μm and up to 10 μm cell wall thickness.

The first transition (Fig. 3a → b) is the soaking of the native wood with ionic liquid. It penetrates the lumen of the material within seconds but the structure is not changed macroscopically (Fig. 3b). The structure becomes however more translucent. This way, the characteristic ray cells of beech wood become visible as horizontal lines in Fig. 3b.

Within the next 45 s, a swelling of the material can be observed (Fig. 3c), which starts on the edges of the chip and is more pronounced in earlywood compared to latewood. In this transition, the cell walls undergo a volume expansion. Afterwards, the tissue starts to disintegrate (> 50 s). Both processes of swelling and disintegration nearly coincide in these thin cuts resulting in complete disintegration after 400 s (Fig. 3d). Nevertheless, the characteristic ray cells can still be identified. It has to be noted that the tissue
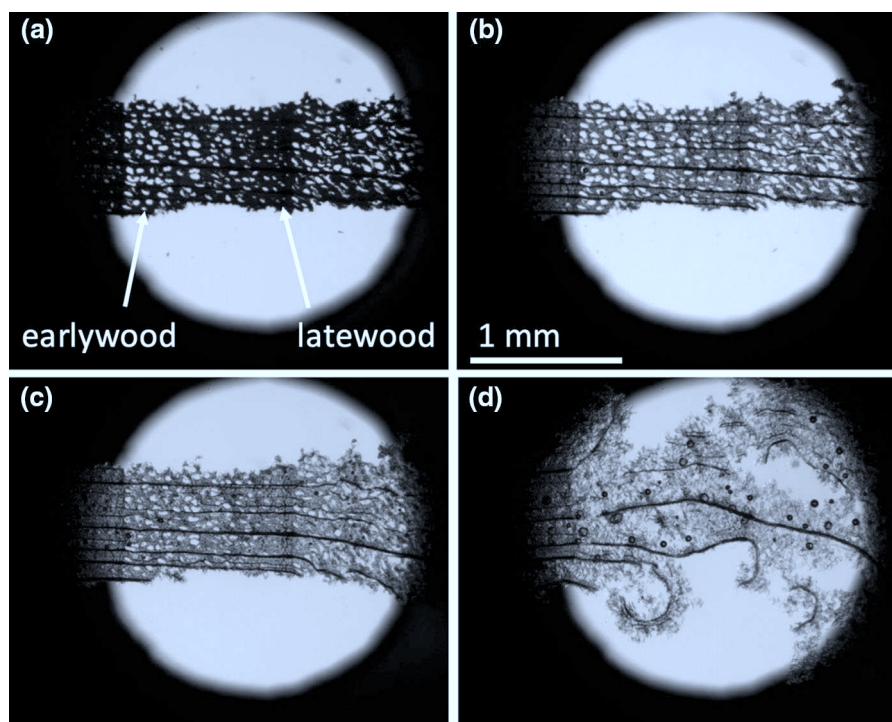
Fig. 3 Radial cut of beech (thickness 60 μm) and the effect of EMIMAc at 95 °C at different times t = 0 s (**a**), 5 s (**b**), 50 s (**c**) and 400 s (**d**). The darker and lighter regions in the middle of the radial cut are due to latewood and earlywood formed during winter and summer, respectively. Full movie available in the supplementary information

is not dissolved but the cell fragments have been disrupted from each other. Small gas bubbles were observed during the experiment.

The observation agrees well to previous reports about the complete disintegration (Viell et al. 2016; Viell and Marquardt 2011; Miyafuji et al. 2009). Further, it can be seen that disintegration of beech wood is stronger in the tangential direction (vertical in Fig. 3) than in the radial direction (horizontal in Fig. 3). The disintegration is obviously related to the volumetric expansion of the material due to the solvation of the ions within the cell wall. It is argued that solvation of microfibrils cause the largest swelling normal to the cell wall. Hence, the disintegration of the material is likely connected with cellulose solvation and swelling that causes this macroscopic effect. However, the optical analysis cannot resolve the scale of polymer interaction, which is to be analyzed by in operando SANS studies next.

SANS

In operando SANS measurements were carried out with deuterated EMIMAc to increase the contrast of the solvent penetrating the matrix of carbohydrates and lignin. 2-dimensional scattering patterns of the IL pretreated wood at smallest scattering angles (i.e., 20 m detector distance, Fig. 4) show a clear anisotropy that decays with increasing time. The first picture after 60 min (Fig. 4a) shows a rectangular pattern that evidences a regular order in both meridional and equatorial direction. Hence, this signal can be assigned to the organization of the cell walls. During the experiment, this pattern transforms into a more uniform pattern implying a loss of anisotropy. However, the second image still shows a pronounced scattering in the equatorial direction after 130 min. After 250 min, the circular pattern reveals completely circular scattering (Fig. 4c). The structure of wood is thus changed from ordered tissue into an isotropic state.

Shorter detector distances (1.5 and 4 m) reveal the scattering of fibrils and the cell wall. Figure 5 shows
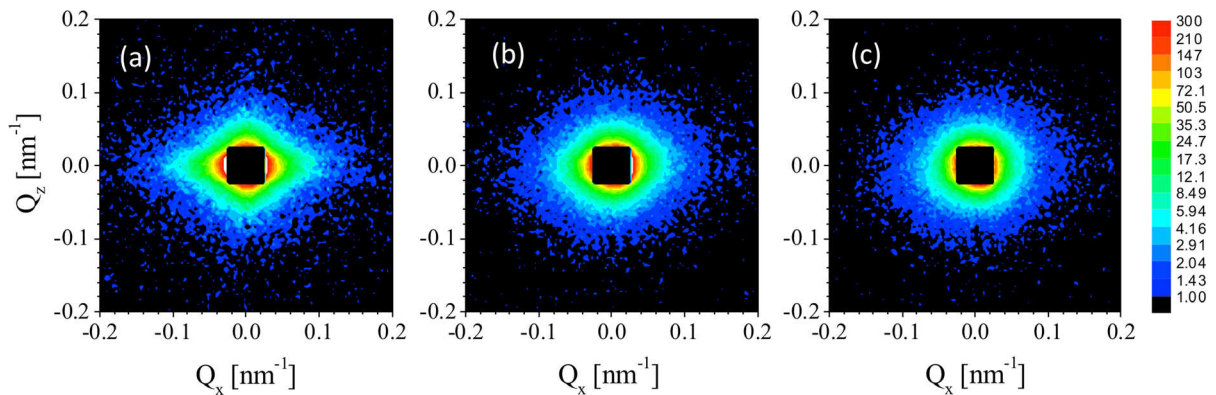
Fig. 4 The scattering intensity at smallest angles (20 m detector distance) results from cell walls in IL after **a** 60 min, **b** 130 min and **c** 250 min. At first the scattering clearly shows pronounced intensities along the equatorial and meridional direction. The anisotropy decreases **b** to complete isotropy **c**
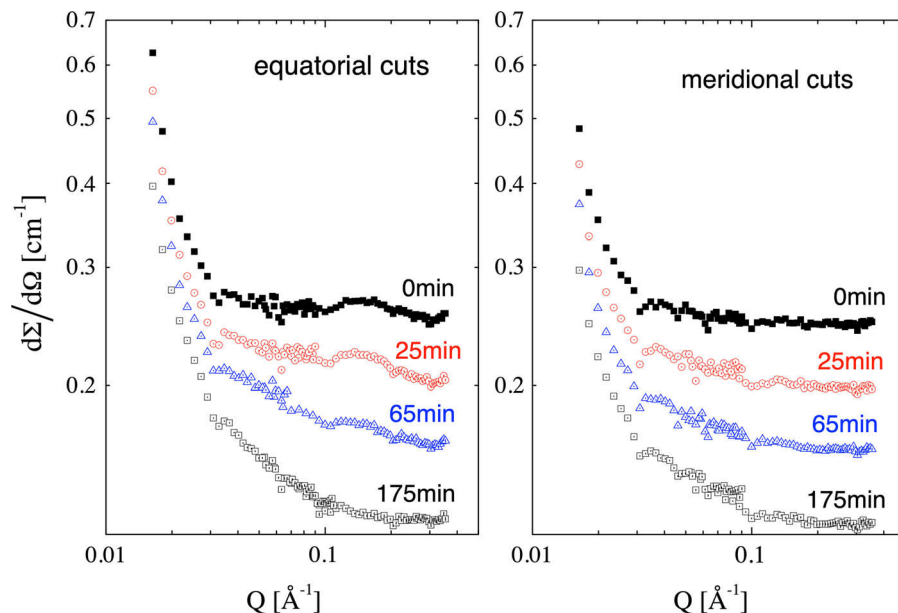
Fig. 5 Line cuts of the scattering patterns at shorter detector distances (concatenated data of 1.5 and 4 m), each plot in chronological order (therefore shifted by a factor of 0.8 for 25 min, 0.64 for 65 min and 0.55 for 175 min). In the equatorial cuts (left) more information about the fibrils is obtained, while the meridional cuts (right) appear to have less structure

line cuts along the equatorial and the meridional directions at different experimental times with intensities on absolute scale versus the scattering vector Q. The steep increase below $Q < 0.04$ Å^{-1} is visible in all experiments and results from the cell wall structure (cf. Nishiyama et al. 2014). It results from the contrast of cell walls against the cells filled with IL. With larger Q, the scattering is governed by fibrils. Thus, the equatorial direction contains more information as a result of a preferred fibril direction close to the meridional axis. In particular, a clear peak at $Q = 0.15$ Å^{-1} is observed at shorter times (0 and 25 min) that is the known scattering of interfibrillar water between the microfibrils of native wood (Murmanis and Chudnoff 1979; Viell et al. 2016). This peak becomes weak after 65 min, and completely vanishes at 175 min.

However, both the equatorial and meridional line cuts show a shoulder at approximately $Q = 0.05$ Å^{-1}, which clearly deviates from the Porod scattering

below $Q < 0.02$ Å^{-1}. This indicates that there is still some structural information which cannot be obtained from averaged line cuts but requires a more sophisticated data evaluation.

Reduced model results

A simple quantitative analysis of isotropy in equatorial and meridional direction is enabled by the order parameters P_4 and P_2 [cf. Eqs. (4), (5)]. They are plotted as a function of time in Fig. 6. With P_4 starting higher than P_2, it demonstrates that there is also a considerable isotropy in longitudinal direction. P_4 decreases from 0.35 rapidly within the first 2 h showing an almost constant trend downwards for up to 110 min. Afterwards, the trend declines to reach its constant minimum at 0.075. P_2 exhibits a dip within the first minutes and only starts to decrease after 100 min. Interestingly, the inflection point of P_4 coincides with the decrease of P_2 suggesting a consecutive mechanism. Such a strong decrease of P_4 has not been observed with sodium hydroxide (NaOH) although being a strong swelling agent. In our experiments with NaOD, the order parameter P_4 along the longitudinal axis is by far not as low as in case of the IL (cf. Fig. 16 and Fig. 15 in SI) nor does it reach lower values than P_2.

The results need to be discussed in view of the structure of wood to gain a first interpretation. First of all, the process time is obviously much longer than observed microscopically. This is plausible due to the much larger size of the sample and the relatively high
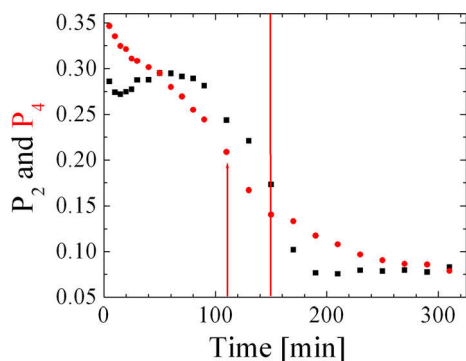
Fig. 6 The anisotropy of the cell wall scattering characterized by the order parameters P_2 (black filled square) and P_4 (red filled circle) as a function of time. The inflection points (marked by the two vertical lines) of P_4 at approx. 110 min P_2 at approx. 150 min correspond to a loss of initial cell wall orientation

viscosity of the IL even at 110 °C. The viscosity-limited transport of IL in wood is further hindered by the vascular structure of intact cells. As they are not cut as in Fig. 3, the liquid has to flow through the available lumen. Consequently, the longitudinal flow via vessels is preferred by an order of magnitude (Siau 1984; Scholz et al. 2010; Fernandes et al. 2011) in comparison to the flow in radial or tangential direction. Hence, the ionic liquid quickly enters the vessels to fill the cell lumen before penetrating the cell walls. As the detector distance of 20 m reveals cell wall scattering, the latter is obvious by the initial dip in P_2 that can be interpreted as penetration of the material with ionic liquid in equatorial direction. Obviously, the well-ordered cells become disturbed by intrusion of the ionic liquid until they relax in a more regular manner. These processes refer to the soaking of the material as observed in Fig. 3a → b.

After 100 min, the equatorial order parameter P_2 starts to decrease to reach eventually a state of complete isotropy on the cellular level at around 200 min corresponding to the completely disintegrated state in Fig. 3d. So far, it is unclear why the meridional order P_4 at this detector distance is decreased so efficiently and is even in advance to the trajectory of P_2 in equatorial direction. This will be analyzed by the detailed scattering model in the following.

Detailed model results

Figure 7 shows the full scattering data in the 2D representation at time points selected to present the largest differences. The scattering in Fig. 7a, b, e, f (0 and 25 min) is governed by the structure of intact fibrils in wood. In comparison, the equatorial signal is even stronger after 25 min, which is due to the higher contrast of the ionic liquid replacing the interfibrillar water. Hence, this characteristic signal is clearly due to the microfibrils in the vertical macrofibrils (Zhang et al. 2005; Viell et al. 2016), where the water and hemicellulose separates the microfibrils in a rather regular 2-dimensional lattice with a repeating distance of approx. 4 nm (Viell et al. 2016; Langan et al. 2014). At later stages (65 and 175 min), the scattering of fibrils diminishes but unveils the weak scattering contribution at lower Q as observed in Fig. 5 already but without interpretation so far.
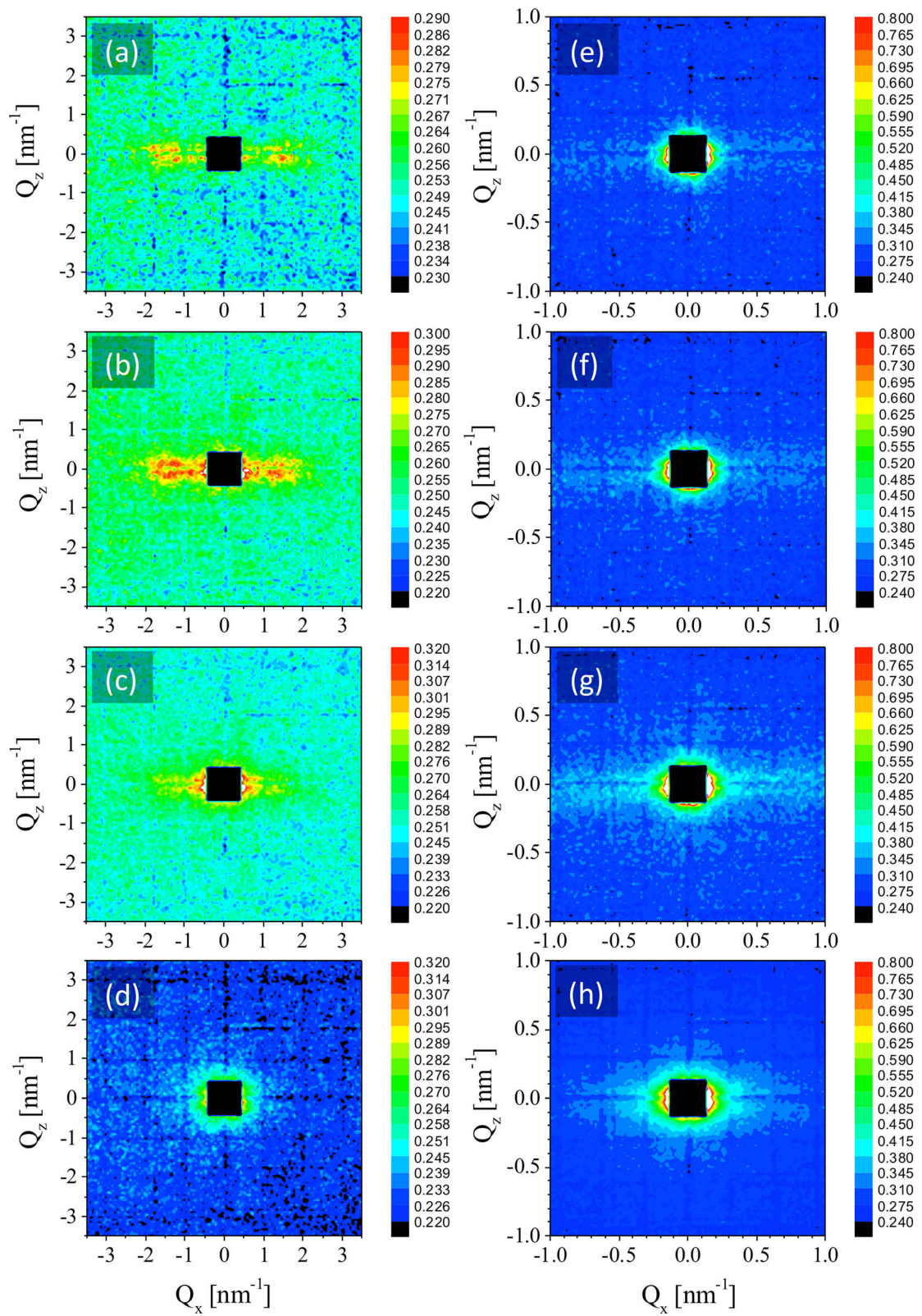
◀ **Fig. 7.** 2D scattering data at detector distances of 1.5 m (**a–d** left column) and 4 m (**e–h** right column) after times of **a, e** 0 min, **b, f** 25 min, **c, g** 65 min and **d, h** 175 min. The visible grid is due to residual margins of the photo multipliers. All intensities are calibrated and compare on absolute scales

Table 1 shows the results of the model fit. The coherence lengths basically show that for the shorter detector distances $\xi_{tot,xy}$ and $\xi_{tot,Z}$ lie in 4 nm range and for the longer detector distance in the 13 nm range, which agrees to the expected resolution as already discussed in the experimental SANS part before. Similarly, the constant incoherent background arising from hydrogen atoms in the irradiated sample volume demonstrates constant measurement conditions. Further parameters can thus be discussed in view of changes in the wooden structure.

The prefactors A_{fibril} and A_{wall} allow for a relative comparison to reveal the contribution of fibrils over cell walls to the scattering. The comparison between 25 and 65 min shows that the prefactor of the fibrils A_{fibril} at 65 min decreases while the wall prefactor A_{wall} is in the same order of magnitude as observed at 25 min. This implies that the scattering volume of the inner fibril structure decreases while the wall geometry has not changed considerably. For the late stage at 175 min, we focused on the 4 m measurement to increase resolution at the much more pronounced upturn at small Q (Figs. 5, 6). For this reason, the amplitude A_{wall} is much larger than at the other time points but A_{fibril} is also clearly lower than A_{wall} which further underpins a decreased density of the fibrillar structure in comparison to the wall. Hence, the walls

show a much larger contrast and fibrils seem to get less and less densely organized.

The concentration η of fibrils shows no considerable change as it is nearly the same value at 25 min and after 175 min. At 65 min, it had to be set to 60% as the structure factor was too small to identify the fibril concentration in the data. As the material is enclosed within the measurement volume, it is plausible to have roughly the same total concentration of fibrils at all experimental data points.

At first glance, it looks puzzling to identify such a strong cell wall contribution in the experimental results. Before we continue with the interpretation of the parameters, we check the data for plausibility by comparing the absolute amplitudes in Table 1 with the structural parameters in the model equations (Eqs. 6–12). The amplitude A_{fibril} is the following product: $\phi_{wall}(\Delta\varrho)^2\eta(1-\eta)V_{fibril}$. The first two factors are constant because the volume fraction of wall volume in the wood ϕ_{wall} is closely connected to the incoherent scattering (background in Table 1) and the contrast of cellulose against deuterated EMIMAc results from the scattering length density difference, which is also constant ($\rho_{cellulose} \approx 1.8$ to 1.9×10^{-4} nm^{-2}, (Chazeau et al. 1999; Velichko et al. 2017; Martínez-Sanz et al. 2016) and ρ_{EMIMAc} = 5.6×10^{-4} nm^{-2}). The product $\eta(1 - \eta)$ reflects the Babinet principle (scattering can arise from liquids or matter) and leaves room for interpretation whether fibrils or holes are considered as dominating structure. From the degree of pronunciation from the structure factor S_{PY} as a peak we obtain a very good estimate of η from our fitting procedure. The volume V_{fibril} reflects the structural volume that appears coherently

Table 1 Parameter values of the fits in Fig. 7 using Eq. 6–12 at individual times of the experiment

Parameters	t = 25 min	t = 65 min	t = 175 min
Meridional coherence length $\xi_{tot,Z}$ (nm)	4.38 ± 0.08	4.2 ± 0.2	14.7 ± 0.2
Equatorial coherence length $\xi_{tot,xy}$ (nm)	3.05 ± 0.11	4.2 ± 0.2	10.2 ± 0.2
Background (cm^{-1})	0.249 ± 0.001	0.252 ± 0.001	0.273 ± 0.001
A_{fibril} (cm^{-1})	0.400 ± 0.009	0.043 ± 0.001	0.279 ± 0.009
A_{wall} (cm^{-1})	0.059 ± 0.003	0.070 ± 0.004	1.239 ± 0.042
Microfibril concentration η (%)	78.0 ± 0.3	60 (set)	82.2 ± 0.3
Cylinder radius R (nm)	1.37 ± 0.01	1.03 ± 0.02	3.18 ± 0.13

Uncertainty values are given if parameters were fitted, otherwise indicated by "set" (cf. Fig. 10 in Supplementary Information for visual fitting results)

in the experiment (over larger distances the objects are uncorrelated). With $V_{fibril} = \pi R^2 L_p$, with L_p being a persistence or correlation length of the objects. With L_p from literature, one can thus compare with A_{fibril}. Ramie shows $L_p = 50$–300 nm (Crawshaw et al. 2002) and a linear cellulose molecule with a molar mass of at least 10^5 g/mol (Klemm et al. 1998) calculates $L_p > 150$ nm (Nishiyama et al. 2003). This corresponds to the state at 25 min in our experiments. The data point after 65 min will be discussed later. After 175 min, we reach the region of $L_p = 10$–20 nm, which agrees to dissolved cellulose (Gupta et al. 1976; Boerstoel et al. 2001). The results (Table 2, line 3) are well proportional with the values of the model (Table 1) and we can state that the amplitude A_{fibril} agrees with the principal assumptions. We estimate that the cellulose fibrils in the whole volume occupy a volume fraction ϕ_{wall} of approx. 6% in the dry wood. In comparison to the values in Table 1 A_{fibril} differs by a constant factor of 20–30, which is acceptable in the measurement of natural materials. Nevertheless, the ratio of A_{fibril} at the individual time points is the constant which proves the physical justification of the fitted parameters in Table 1.

A_{wall} (Table 2, line 4) can only be compared heuristically from the resolution parameters $\xi^2_{tot,xy}$-$\xi_{tot,Z}$. This estimate cannot be given on absolute scale, but satisfies the coarse proportionality.

Much more information on the state of the wooden tissue can be derived from the geometrical parameters of the model. The fibril radius R yields informative data on the state of the fibrillar network. At 25 min, the value of 1.37 nm agrees with the diameter of individual microfibrils that is reported (ranging from 2.4 to 3.6 nm, cf. Martínez-Sanz et al. 2015; Thomas et al. 2014; Jungnikl et al. 2008; Nishiyama et al. 2014; Penttilä et al. 2019). Surprisingly, the radius goes down to approximately 1 nm at 65 min but reaches a much larger value of $R = 3.18$ nm after 175 min. The approximate dimensions of the early (25 min) stage thus has been confirmed but the subsequent process leading to the intermediate (65 min) and late (175 min) values needs to be discussed thoroughly. Theoretically, any dissolution of hemicellulose could lead to a smaller net diameter of microfibrils (calculated as center-to-center distance) but the experimental results of the composition (Viell et al. 2016) and the lattice spacing of approximately 8×3 or 6×4 cellulose chains within the microfibril (Fernandes et al. 2011; Thomas et al. 2014) make such a small diameter very unlikely. Furthermore, this would imply shrinking of the material, which has neither been observed macroscopically nor by microscopy (cf. Fig. 3). Effects of deuteration of the outer molecules of a crystalline core have been reported (Loelovitch and Gordeev 1994) but would cause a much smaller effect. Hence, the 1 nm structure unlikely originates from cellulose microfibrils.

Another possibility is the formation of voids within the microfibrils. According to the Babinet's principle (Glatter and Kratky 1982), a scattering signal cannot be differentiated for either matter of higher density or voids filled up with liquid but of lower density. Native wood shows a void diameter of approximately 6 nm (Sawada et al. 2018) similar to ramie cellulose fibers (Crawshaw et al. 2002). The native pore volume fraction is around 10% (Grethlein 1985). In fact, the analysis of beech wood in this study does not exhibit this length scale but it seems to be hidden behind the stronger Porod scattering (cf. supplementary information). Hence, the detected radii point towards voids that are newly-formed in the system of cellulose fibrils.

The origin of these voids can be hypothesized by the structure of the native cellulose microfibril. In native state, it almost entirely consists of crystalline

Table 2 Verification of the absolute scattering intensities from the experimentally determined magnitudes

Parameters	t = 25 min	t = 65 min	t = 175 min
L_p (nm)	50–300	16–24	10–20
$(\Delta\rho)^2 \phi_{wall} \eta (1 - \eta) \pi R^2 L_p$ (cm^{-1}), i.e. estimated A_{fibril}	4.2–26	1.1–1.6	3.9–7.8
$\xi^2_{tot,xy} \xi_{tot,Z} \times 0.001$ (nm^3) as estimate for A_{wall}	0.06	0.07	2.2

While A_{fibril} is compared on absolute scale, the heuristic formula for A_{wall} is highly semiquantitative. The persistence lengths result from estimations given in the text

cellulose chains (Nishiyama 2009) but it contains defects of periodic nature (Nishiyama et al. 2003) at about 1.5% volume fraction. These defects are plausible entry points for the ions of EMIMAc, as has been shown to be the case with other chemical treatments as well (Nishiyama 2009), in parallel with the dissolution of intercalated matrix polymers and the native voids. As a plausibility check, a void length of Lp between 16 and 24 nm (as obtained after alkaline treatment, cf. Crawshaw et al. 2002) agrees well to the surface of A_{fibril}. So, the IL treatment results in an increasing fraction of small voids.

After 175 min, the increased diameter of 6.4 nm is much bigger than a single microfibril. Its increase in radius can be interpreted twofold. Since the cladding of the microfibril is altered due to the effect of the ionic liquid, microfibrils could coalesce with other microfibrils to form larger fibrillar structures. Such a process with increasing crystalline cellulose has been observed under acidic conditions (Silveira et al. 2016; Yao et al. 2018a, b), after pulping (Fahlén and Salmén 2005) and for the transformation to other cellulose polymorphs (Chundawat et al. 2020).

The second explanation of the increasing diameter is based the liquid ions penetrating and swelling the microfibril. Molecular dynamic simulations have shown the bulky and flat imidazolium cations of the IL to wedge into the cellulose bundles (Rabideau et al. 2013) in contrast to very mobile mono-atomic ions. This interpretation thus suggests a volume expansion of the material, which is in line with Fig. 3 and the observation of more amorphous material after pretreatment with EMIMAc. The diameter of 6.4 nm thus likely corresponds to swollen fibrils that might have also coalesced. In combination with the microscopic results of disintegration by volume expansion, the penetration and swelling of fibrils in combination with coalescence seems plausible.

The mechanism of pretreatment with the IL thus starts with longitudinal transport of EMIMAc in the cells and diffusion into the cell wall. There, the fibrils are subject to the formation of voids, which are entry points for the ions. Next, the ions wedge along the cellulose fibrils for decrystallization and coalescence. In addition to simple volume expansion by solvating ions, the contraction of the fibril has been observed during mercerization (Lonikar et al. 1984; Nakano and Nakano 2015; Nakano et al. 2013; Revol and Goring 1981). It is known that this fibril contraction applies

force rectangular to the cell walls (Nakano and Nakano 2014), which is further promoted by volumetric expansion in equatorial direction due to the solvation by bulky ions. The contraction likely starts already before 65 min as it increases the number of defects per volume. The combination of these effects with a weakened intercellular adhesion likely leads to disintegration of the material as observed in Fig. 3.

After this analysis, the pretreatment with EMIMAc can be monitored in operando to differentiate between three different states: First, the state at 25 min with elementary chains of approximately 1 nm as the governing longitudinal structure, second, the presence of voids due to the action of pretreatment (65 min) and third, the swollen or coalesced fibrils after 175 min. To this end, the different amplitudes A_{25}, A_{65}, A_{175} can be normalized to the maximum amplitude of the respective state for comparability. Such superposition is achieved using the following equation:

$$\frac{d\Sigma_{tot}}{d\Omega} = A_{25}\left(\frac{d\Sigma_{\text{fibril}}}{d\Omega} + \frac{d\Sigma_{\text{wall}}}{d\Omega}\right)_{25\text{min}}$$
$$+ A_{65}\left(\frac{d\Sigma_{\text{fibril}}}{d\Omega} + \frac{d\Sigma_{\text{wall}}}{d\Omega}\right)_{65\text{min}}$$
$$+ A_{175}\left(\frac{d\Sigma_{\text{fibril}}}{d\Omega} + \frac{d\Sigma_{\text{wall}}}{d\Omega}\right)_{175\text{min}} + \{\text{background}\}$$
$$(13)$$

Figure 8 summarizes the trends of these amplitudes and suggests 3 stages of the pretreatment. Intact microfibrils of native wood are present at times below 55 min with continuous decrease. It coincides with penetration of the ionic liquid into the material and
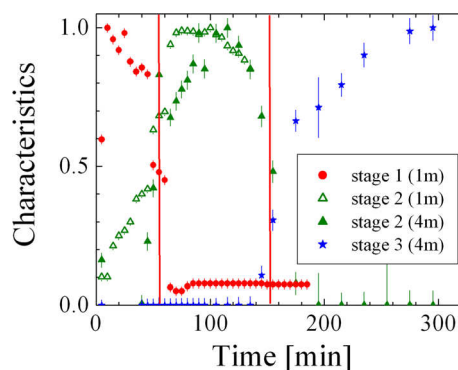
Fig. 8 The normalized characteristics of the scattering pattern as a function of time. Clearly visible are the penetration of native wood, the formation of voids predominantly after 55 min, and the swelling of fibrils after 150 min

represents stage 1. In stage 2, the effect of the ionic liquid creates or enhances small voids, of which formation is justified independently at 1.5 m and 4 m detector distance. Next, the third stage after 150 min is characterized by the swelling of microfibrils which results eventually in amorphous material (Doherty et al. 2010). In parallel, the material disintegrates. Hence, the stages of (1) penetration, (2) formation of voids along the longitudinal fibrils in wood, and (3) the subsequent fibril swelling and coalescence are suggested as the inherent stages leading to macroscopic disintegration during pretreatment with ionic liquid. This precise analysis now enables to utilize simple models like order parameters (i.e., Fig. 6) for facile monitoring of pretreatment processes in operando.

To challenge the suggested interpretation, reference experiments with NaOD have been carried out (see supplementary information). While excessive swelling of cellulose is well known in NaOD, there is no macroscopic disintegration and also the enzymatic digestibility of wood after pretreatment with NaOD is by far inferior to the pretreatment with EMIMAc. Remarkably, neither the delignified nor the native wood reach a low order number as observed in EMIMAc. This implies that the formation of voids and the reduction of order is a viable measure to monitor the pretreatment in operando.

Summary

This study presents structural changes of lignocellulosic biomass during pretreatment in ionic liquids monitored in operando and at different length scales. In addition to microscopy, detailed 2D scattering models have been applied to in operando SANS data in order to understand the phenomena during pretreatment of beech wood in EMIMAc. The gained insight is discussed in comparison with a model of reduced complexity to enable in operando monitoring of pretreatment.

The article shows in operando SANS data of pretreatment with an IL for the first time. The analysis of a wood pretreatment in EMIMAc results in three different stages according to the identified structural features: The first stage exhibits a signal of native wood dominated by microfibrils of 2.7 nm distance that are impregnated with the liquid. The next stage is then dominated by less ordered microfibrils and newly-formed voids of 1 nm radius. Then, the microfibrils form swollen but amorphous cellulose with strands of 3.2 nm radius that likely also includes coalescence of some microfibrils. These stages of impregnation, formation of voids and swelling with macroscopic disintegration seem to be characteristic for the process in EMIMAc. Prior to disintegration, the voids or disorder along the fibrils (i.e., meridional direction) seem to be a precondition for IL entry that cannot be observed in alkaline pretreatment, which does not result in disintegration. The simple analysis of our SANS experiments by order parameters might enable easier analysis and faster pretreatment development in biomass conversion processes.

References

Baker DA, Rials TG (2013) Recent advances in low-cost carbon fiber manufacture from lignin. J Appl Polym Sci 130:713–728

Billès E, Onwukamike KN, Coma V, Grelier S, Peruch F (2016) Cellulose oligomers production and separation for the synthesis of new fully bio-based amphiphilic compounds. Carbohyd Polym 154:121–128

Boerstoel H, Maatman H, Westerink JB, Koenders BM (2001) Liquid crystalline solutions of cellulose in phosphoric acid. Polymer 42(17):7371–7379

Börner HG, Smarsly BM, Hentschel J, Rank A, Schubert R, Geng Y, Discher DE, Hellweg T, Brandt A (2008) Organization of self-assembled peptide−polymer nanofibers in solution. Macromolecules 41(4):1430–1437

Chazeau L, Cavaillé JY, Terech P (1999) Mechanical behaviour above Tg of a plasticised PVC reinforced with cellulose whiskers; a SANS structural study. Polymer 40(19):5333–5344

Chen S, Ling Z, Zhang X, Kim YS, Xu F (2018) Towards a multi-scale understanding of dilute hydrochloric acid and mild 1-ethyl-3-methylimidazolium acetate pretreatment for improving enzymatic hydrolysis of poplar wood. Ind Crops Prod 114:123–131

Chundawat SPS, da Costa SL, Roy S, Yang Z, Gupta S, Pal R, Zhao C, Liu S-H, Petridis L, O'Neill H, Pingali SV (2020) Ammonia-salt solvent promotes cellulosic biomass deconstruction under ambient pretreatment conditions to enable rapid soluble sugar production at ultra-low enzyme loadings. Green Chem. https://doi.org/10.1039/C9GC03524A

Crawshaw J, Bras W, Mant GR, Cameron RE (2002) Simultaneous SAXS and WAXS investigations of changes in native cellulose fiber microstructure on swelling in aqueous sodium hydroxide. J Appl Polym Sci 83(6):1209–1218. https://doi.org/10.1002/app.2287

Doherty TV, Mora-Pale M, Foley SE, Linhardt RJ, Dordick JS (2010) Ionic liquid solvent properties as predictors of lignocellulose pretreatment efficacy. Green Chem 12(11):1967–1975. https://doi.org/10.1039/C0GC00206B

Ebringerová A, Hromadková Z (1989) Alternative Verfahren zur Gewinnung von Hemicellulosen des D-Xylantyps aus Laubhölzern. Holz Roh Werkst 47:355–358. https://doi.org/10.1007/BF02606031

Fahlén J, Salmén L (2005) Ultrastructural changes in a holocellulose pulp revealed by enzymes, thermoporosimetry and atomic force microscopy. Holzforschung 59:589–597

Feiging LA, Svergun DI (1987) Structure analysis by small-angle X-ray and neutron scattering. Plenum Press, New York

Fengel D, Wegener G (1989) Wood: chemistry, ultrastructure, reactions. de Gruyter, Berlin

Feoktystov AV, Frielinghaus H, Di Z, Jaksch S, Pipich V, Appavou M, Brückel T (2015) KWS-1 high-resolution small-angle neutron scattering instrument at JCNS: current state. J Appl Cryst 48:61–70

Fernandes AN, Thomas LH, Altaner CM, Callow P, Forsyth VT, Apperley DC, Jarvis MC (2011) Nanostructure of cellulose microfibrils in spruce wood. PNAS 108(47):1195–1203

Frielinghaus H, Feoktystov A, Berts I, Mangiapia G (2015) KWS-1: small-angle scattering diffractometer. J Large Scale Res Facil 1(A28):1–4. https://doi.org/10.17815/jlsrf-1-26

Glatter O, Kratky O (1982) Small angle x-ray scattering. Academic Press Inc Ltd, London

Grethlein HE (1985) The effect of pore size distribution on the rate of enzymatic hydrolysis of cellulose substrates. Biotechnology 3:155–160

Gupta AK, Cotton JP, Marchal E, Burchard W, Benoit H (1976) Persistence length of cellulose tricarbanilate by small-angle neutron scattering. Polymer 17(5):363–366

Jungnikl K, Paris O, Fratzl P, Burgert I (2008) The implication of chemical extraction treatments on the cell wall nanostructure of softwood. Cellulose 15:407–418. https://doi.org/10.1007/s10570-007-9181-5

Klemm D, Philpp B, Heinze T, Heinze U, Wagenknecht W (1998) Comprehensive cellulose chemistry. Volume 1: fundamentals and analytical methods. Wiley, Hoboken

Kontturi E (2006) Cellulose-model films and the fundamental approach. Chem Soc Rev 35(12):1287–1304

Langan P, Petridis L, O'Neill HM, Pingali SV, Foston M, Nishiyama Y, Davison BH (2014) Common processes drive the thermochemical pretreatment of lignocellulosic biomass. Green Chem 16:63–68. https://doi.org/10.1039/C3GC41962B

Lee SH, Doherty TV, Linhardt RJ, Dordick JS (2009) Ionic liquid–mediated selective extraction of lignin from wood leading to enhanced enzymatic cellulose hydrolysis. Biotechnol Bioeng 102:1368–1376

Li Y, Wang J, Liu X, Zhang S (2018) Towards a molecular understanding of cellulose dissolution in ionic liquids: anion/cation effect, synergistic mechanism and physicochemical aspects. Chem Sci 9:4027–4043. https://doi.org/10.1039/C7SC05392D

Loelovitch M, Gordeev M (1994) Crystallinity of cellulose and its accessibility during deuteration. Acta Polym 45(2):121–123. https://doi.org/10.1002/actp.1994.010450211

Lonikar SV, Yokota T, Higuchi T (1984) Effect of the loosening of wood texture on the mercerization of cellulose in wood. J Wood Chem Technol 4(4):483–496

Martínez-Sanz M, Gidley MJ, Gilbert EP (2015) Application of X-ray and neutron small angle scattering techniques to study the hierarchical structure of plant cell walls: a review. Carbohyd Polym 125:120–134

Martínez-Sanz M, Gidley MJ, Gilbert EP (2016) Hierarchical architecture of bacterial cellulose and composite plant cell wall polysaccharide hydrogels using small angle neutron scattering. Soft Matter 12:1534–1549

Miyafuji H, Miyata K, Saka S, Ueda F, Mori M (2009) Reaction behavior of wood in an ionic liquid, 1-ethyl-3-methylimidazolium chloride. J Wood Sci 15:215–219

Mohanty AK, Wibowo A, Misra M, Drzal LT (2003) Development of renewable resource-based cellulose acetate bioplastic: effect of process engineering on the performance of cellulosic plastics. Polym Eng Sci 43:1151–1161. https://doi.org/10.1002/pen.10097

Mosier N, Wyman C, Dale B, Elander R, Lee YY, Holtzapple M, Ladisch M (2005) Features of promising technologies for pretreatment of lignocellulosic biomass. Bioresour Technol 96(6):673–686

Moulthrop JS, Swatloski RP, Moyna G, Rogers RD (2005) High–resolution ^{13}C NMR studies of cellulose and cellulose oligomers in ionic liquid solutions. Chem Commun 12:1557–1559

Murmanis L, Chudnoff M (1979) Lateral flow in beech and birch as revealed by the electron microscope. Wood Sci Technol 13(2):79–87. https://doi.org/10.1007/BF00368601

Nakano S, Nakano T (2014) Change in circularity index of cell lumen in a cross-section of wood induced by aqueous NaOH. J Wood Sci 60(2):99–104. https://doi.org/10.1007/s10086-013-1382-y

Nakano S, Nakano T (2015) Morphological changes induced in wood samples by aqueous NaOH treatment and their effects on the conversion of cellulose I to cellulose II. Holzforschung 69(4):483–491

Nakano T, Tanimoto T, Hashimoto T (2013) Morphological change induced with NaOH–water solution for ramie fiber: change mechanism and effects of concentration and temperature. J Mater Sci 48(21):7510–7517. https://doi.org/10.1007/s10853-013-7565-5

Niaounakis M (2013) Biopolymers: reuse, recycling, and disposal. Elsevier, Oxford

Nishiyama Y (2009) Structure and properties of the cellulose microfibril. J Wood Sci 55(4):241–249

Nishiyama Y, Kim U-J, Kim D-Y, Katsumata KS, May RP, Langan P (2003) Periodic disorder along ramie cellulose microfibrils. Biomacromol 4(4):1013–1017. https://doi.org/10.1021/bm025772x

Nishiyama Y, Langan P, O'Neill H, Pingali SV, Harton S (2014) Structural coarsening of aspen wood by hydrothermal pretreatment monitored by small- and wide-angle scattering of X-rays and neutrons on oriented specimens. Cellulose 21(2):1015–1024

Pedersen JS, Posselt D, Mortensen K (1990) Analytical treatment of the resolution function for small-angle scattering. J Appl Cryst 23(4):321–333

Penttilä PA, Rautkari L, Österberg M, Schweins R (2019) Small-angle scattering model for efficient characterization of wood nanostructure and moisture behaviour. J Appl Cryst 52:369–377

Petridis L, Pingali SV, Urban V, Heller WT, O'Neill HM, Foston M, Smith JC (2011) Self-similar multiscale structure of lignin revealed by neutron scattering and molecular dynamics simulation. Phys Rev E Stat Nonlinear Soft Matter Phys 83(6 Pt 1):061911

Pihlajaniemi V, Sipponen MH, Pastinen O, Lehtomäkia I, Laaksoa S (2015) Yield optimization and rational function modelling of enzymatic hydrolysis of wheat straw pretreated by NaOH-delignification, autohydrolysis and their combination. Green Chem 17:1683–1691

Pingali SV, Urban VS, Heller WT, McGaughey J, O'Neill HM, Foston M, Evans BR (2010a) SANS study of cellulose extracted from switchgrass. Acta Crystallogr D Biol 66(11):1189–1193

Pingali SV, Urban VS, Heller WT, McGaughey J, O'Neill H, Foston M, Evans BR (2010b) Breakdown of cell wall nanostructure in dilute acid pretreated biomass. Biomacromol 11(9):2329–2335

Pingali SV, O'Neill HM, McGaughey J, Urban VS, Rempe CS, Petridis L, Heller WT (2011) Small angle neutron scattering reveals pH-dependent conformational changes in *Trichoderma reesei* cellobiohydrolase I: implications for enzymatic activity. J Biol Chem 286:32801–33280

Plaza NZ, Pingali SV, Qian S, Heller WT, Jakes JE (2016) Informing the improvement of forest products durability using small angle neutron scattering. Cellulose 23(3):1593–1607. https://doi.org/10.1007/s10570-016-0933-y

Rabideau BD, Agarwal A, Ismail AE (2013) Observed mechanism for the breakup of small bundles of cellulose Ialpha and Ibeta in ionic liquids from molecular dynamics simulations. J Phys Chem B 117(13):3469–3479

Revol J-F, Goring DA (1981) On the mechanism of the mercerization of cellulose in wood. J Appl Polym Sci 26(4):1275–1282

Rosenfeld Y (1990) Free-energy model for the inhomogeneous hard-sphere fluid in D dimensions: Structure factors for the hard-disk (D = 2) mixtures in simple explicit form. Phys Rev A 42(10):5978–5982

Sawada D, Kalluri UC, O'Neill H, Urban V, Langan P, Davison B, Pingali SV (2018) Tension wood structure and morphology conducive for better enzymatic digestion. Biotechnol Biofuels 11:44

Scholz G, Krause A, Militz H (2010) Exploratory study on the impregnation of Scots pine sapwood (*Pinus sylvestris* L.) and European beech (*Fagus sylvatica* L.) with different hot melting waxes. Wood Sci Technol 44(3):379–388. https://doi.org/10.1007/s00226-010-0353-3

Siau JF (1984) Transport processes in wood. Springer, Berlin

Silveira RL, Stoyanov SR, Kovalenko A, Skaf MS (2016) Cellulose aggregation under hydrothermal pretreatment conditions. Biomacromol 19:2582–2590

Song Y, Zhang J, Zhang X, Tan T (2015) The correlation between cellulose allomorphs (I and II) and conversion after removal of hemicellulose and lignin of lignocellulose. Bioresour Technol 193:164–170

Sun N, Rahman M, Qin Y, Maxim ML, Rodríguez H, Rogers RD (2009) Complete dissolution and partial delignification of wood in the ionic liquid 1-ethyl-3-methylimidazolium acetate. Green Chem 11:646–655

Tecnaro (2019) Tecnaro. https://www.tecnaro.de/anwendungen.html. Accessed 29 July 2019

Thomas LH, Forsyth VT, Martel A, Grillo I, Altaner CM, Jarvis MC (2014) Structure and spacing of cellulose microfibrils in woody cell walls of dicots. Cellulose 21(6):3887–3895. https://doi.org/10.1007/s10570-014-0431-z

Velichko EV, Buyanov AL, Saprykina NN, Chetverikov YO, Duif CP, Bouwman WG, Smyslov RY (2017) High-strength bacterial cellulose–polyacrylamide hydrogels: mesostructure anisotropy as studied by spin-echo small-angle neutron scattering and cryo-SEM. Eur Polym J 88:269–279

Viell J, Marquardt W (2011) Disintegration and dissolution kinetics of wood chips in ionic liquids. Holzforschung 65(4):519–525

Viell J, Inouye H, Szekely NK, Frielinghaus H, Marks C, Wang Y, Makowski L (2016) Multi-scale processes of beech wood disintegration and pretreatment with 1-ethyl-3-methylimidazolium acetate/water mixtures. Biotechnol Biofuels 9(1):1–15. https://doi.org/10.1186/s13068-015-0422-9

Wada M, Ike M, Tokuyasu K (2010) Enzymatic hydrolysis of cellulose I is greatly accelerated via its conversion to the cellulose II hydrate form. Polym Degrad Stab 95:543–548

Wang S, Zhao W, Lee TS, Singer SW, Simmons BA, Singh S, Yuan Q (2018) Dimethyl sulfoxide assisted ionic liquid pretreatment of switchgrass for isoprenol production. ACS Sustain Chem Eng 6:4354–4361

Yao K, Wu Q, An R, Meng W, Ding M, Li B (2018a) Hydrothermal pretreatment for deconstruction of plant cell wall: part I. Effect on lignin-carbohydrate complex. AIChE J 64:1938–1953

Yao K, Wu Q, An R, Meng W, Ding M, Li B, Yuan Y (2018b) Hydrothermal pretreatment for deconstruction of plant cell

wall: part II. Effect on cellulose structure and bioconversion. AIChE J 64:1954–1964

Zhang H, Wu J, Zhang J, He J (2005) 1-Allyl-3-methylimidazolium chloride room temperature ionic liquid: a new and powerful nonderivatizing solvent for cellulose. Macromolecules 38:8272–8277